

High-Pressure-Sintering-Induced Microstructural Engineering for an Ultimate Phonon Scattering of Thermoelectric Half-Heusler Compounds

Ran He, Taishan Zhu, Pingjun Ying, Jie Chen, Lars Giebeler, Uta Kühn, Jeffrey C. Grossman,* Yumei Wang,* and Kornelius Nielsch*

Thermal management is of vital importance in various modern technologies such as portable electronics, photovoltaics, and thermoelectric devices. Impeding phonon transport remains one of the most challenging tasks for improving the thermoelectric performance of certain materials such as half-Heusler compounds. Herein, a significant reduction of lattice thermal conductivity (κ_L) is achieved by applying a pressure of ≈ 1 GPa to sinter a broad range of half-Heusler compounds. Contrasting with the common sintering pressure of less than 100 MPa, the gigapascal-level pressure enables densification at a lower temperature, thus greatly modifying the structural characteristics for an intensified phonon scattering. A maximum κ_L reduction of $\approx 83\%$ is realized for HfCoSb from 14 to $2.5 \text{ W m}^{-1} \text{ K}^{-1}$ at 300 K with more than 95% relative density. The realized low κ_L originates from a remarkable grain-size refinement to below 100 nm together with the abundant in-grain defects, as determined by microscopy investigations. This work uncovers the phonon transport properties of half-Heusler compounds under unconventional microstructures, thus showing the potential of high-pressure compaction in advancing the performance of thermoelectric materials.

largely represented by its figure of merit (zT), $zT = S^2\sigma T/\kappa$, where S , σ , T , and κ are the Seebeck coefficient, electrical conductivity, absolute temperature, and the thermal conductivity, respectively. The thermal conductivity ($\kappa = \kappa_e + \kappa_L$) originates from charge carriers (κ_e) and phonons (κ_L). Suppressing phononic transport has been one of the most widely employed strategies to enhance the thermoelectric materials' zT as it avoids the complications in optimizing the intertwined electronic transport properties.^[3,4] The phonon-transport property can be engineered by adjusting the synthesis conditions to tailor the materials' microstructural characteristics. For example, Pan et al. employed a melt-centrifugation technique to produce high-density dislocation arrays and large porosity in p-type $(\text{Bi,Sb})_2\text{Te}_3$.^[5] These pores and dislocations collectively reduced the κ_L by $\approx 60\%$ which ultimately yields an enhanced zT .


In another example, Li et al. applied an atomic layer deposition (ALD) technique to grow ZnO thin layers that cover the $(\text{Bi,Sb})_2\text{Te}_3$ powders.^[6] The ALD-treated powders were subsequently sintered, forming a $(\text{Bi,Sb})_2\text{Te}_3$ -ZnO core-shell structure that yields a reduced thermal conductivity. These works

1. Introduction

The solid-state thermoelectric technology can be applied for certain scenarios such as powering wireless sensors^[1] or spot cooling.^[2] The performance of thermoelectric materials is

Dr. R. He, Dr. P. Ying, Dr. L. Giebeler, Dr. U. Kühn, Prof. K. Nielsch
Leibniz Institute for Solid State and Materials Research
01069 Dresden, Germany
E-mail: k.nielsch@ifw-dresden.de
Dr. T. Zhu, Prof. J. C. Grossman
Department of Materials Science and Engineering
Massachusetts Institute of Technology
Cambridge, MA 02139, USA
E-mail: jcg@mit.edu

J. Chen, Prof. Y. Wang
Beijing National Laboratory for Condensed Matter Physics
Institute of Physics
Chinese Academy of Sciences
Beijing 100190, China
E-mail: wangym@iphy.ac.cn
Prof. K. Nielsch
Institute of Materials Science
Technical University of Dresden
01062 Dresden, Germany
Prof. K. Nielsch
Institute of Applied Physics
Technical University of Dresden
01062 Dresden, Germany

 The ORCID identification number(s) for the author(s) of this article can be found under <https://doi.org/10.1002/sml.202102045>.

© 2021 The Authors. Small published by Wiley-VCH GmbH. This is an open access article under the terms of the Creative Commons Attribution-NonCommercial-NoDerivs License, which permits use and distribution in any medium, provided the original work is properly cited, the use is non-commercial and no modifications or adaptations are made.

DOI: 10.1002/sml.202102045

demonstrated the potential of microstructural engineering in intensifying the phonon scattering.

Other than (Bi,Sb)₂Te₃, microstructural engineering applies to other materials for phonon scattering.^[7–10] Among the widely studied thermoelectric materials, half-Heusler compounds are particularly promising due to their unique advantages such as a high power factor,^[11–14] or mechanical and chemical robustness,^[15,16] employment of abundant and nontoxic elements, etc. On the other hand, these compounds usually possess a large κ_L that hinders their zT improvement.^[17] For example, the κ_L of pristine ZrCoSb is $\approx 21 \text{ W m}^{-1} \text{ K}^{-1}$ at 300 K,^[18] much larger than that of nanostructured Bi₂Te₃ ($\approx 0.9 \text{ W m}^{-1} \text{ K}^{-1}$)^[19] or nanostructured MgAgSb ($\approx 0.6 \text{ W m}^{-1} \text{ K}^{-1}$).^[20] Therefore, the efforts to improve the half-Heusler compounds have mainly been focused on reducing the κ_L during the past decades, where the most effective approach is to introduce 0D point defects. This approach yields zT enhancement for a variety of materials including (V/Nb/Ta)FeSb,^[11,21–24] (Ti/Zr/Hf)Co(Sb/Bi),^[25–31] (Ti/Zr/Hf)Ni(Sn,Pb),^[12,26,32,33] and (Nb/Ta)CoSn.^[34–36] Recently, we reported that point-defect scattering has been the major phonon scattering mechanism of half-Heusler compounds other than the intrinsic phonon–phonon interaction, whereas scattering from other defects is less pronounced.^[18] The insufficient contributions from the higher-dimension defects (such as 2D grain boundaries) greatly attenuated the scattering intensity of phonons, especially at lower frequencies that carry the most heat.

Herein, we report a significantly reduced lattice thermal conductivity for half-Heusler compounds upon engineering the microstructures through high-pressure sintering at $\approx 1 \text{ GPa}$, contrasting the common sintering conditions with $< 100 \text{ MPa}$. The materials studied here include five Sb-based stoichiometric (TiCoSb, ZrCoSb, HfCoSb, NbFeSb, and TaFeSb), three Sn-based stoichiometric (ZrNiSn, TiNiSn, and NbCoSn), and two partially substituted compounds (ZrCoSb_{0.8}Sn_{0.2} and Zr_{0.7}Ti_{0.3}CoSb). The sintering pressure, enhanced by more than one order of magnitude, enables a reduced temperature of 923 K to reach full compaction with a relative density exceeding 95%, contrasting the commonly needed 1200–1500 K. For clarity, we label the sintering condition of 1 GPa and 923 K as “HP,” whereas the compounds sintered at lower pressures ($< 100 \text{ MPa}$) but with a higher temperature are labeled as “HT.” The compared sintering schematics are shown in **Figure 1**. The HP approach is found to drastically reduce the κ_L for almost all previously defined compositions. Microscopic studies are subsequently applied to clarify the origins of the κ_L reduction, which evidence a structural intricacy including a remarkable grain refinement to the sub-100 nm level (2D defects) and a shared occupation of 4c and 4d lattice sites (0D defects). By applying the phonon transport model with a BvK–Debye dispersion,^[18] we uncover a synergistic phonon scattering by these defects, thus showing the potential of high-pressure sintering in engineering the microstructures to modify the phonon transport and improve the thermoelectric performance.

2. Experimental Section

The half-Heusler powders synthesized in this work were prepared through either arc melting the raw elements following a

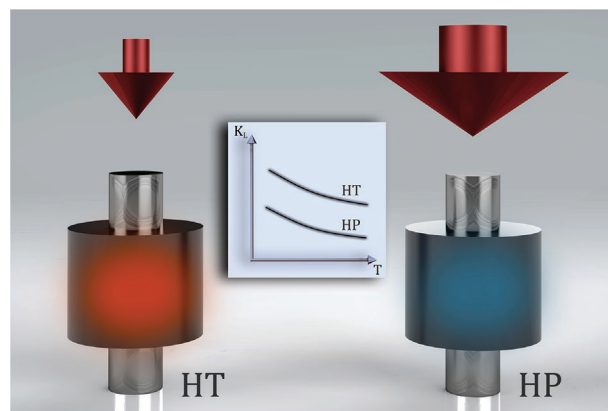


Figure 1. The schematics of different sintering conditions and the effect of high-pressure sintering in reducing the lattice thermal conductivity. The labels HT and HP represent “high temperature” and “high pressure,” respectively.

high energy ball milling (SPEX 8000D), or mechanical alloying via ball milling. The ball millings were performed in stainless steel jars with 2 tungsten carbide balls ($\phi 12 \text{ mm}$). The obtained powders were subject to sintering with either a high temperature plus a lower pressure, or with a higher pressure ($\approx 1 \text{ GPa}$) and a low temperature (923 K). The synthesis details can be found in **Table 1**.

Room-temperature X-ray diffraction patterns were measured in a Bruker D8 Advance diffractometer (Co $K_{\alpha 1}$ radiation) to characterize the phases in Bragg–Brentano geometry. A scanning electron microscope (SEM) was employed to characterize the morphology of broken surfaces. The specimens for transmission

Table 1. The synthesis details of the half-Heusler compounds in this work. Note that the HT sintering details of TiCoSb and TiNiSn are from refs. [12,56]. The HT compounds ZrCoSb, Zr_{0.7}Ti_{0.3}CoSb, and ZrCoSb_{0.8}Sn_{0.2} are from our previous study.^[18]

Compounds	Arc melting	Ball milling	HP sintering	HT sintering
HfCoSb	Yes	2 h	923 K, $\approx 1 \text{ GPa}$, 30 min	1473 K, 50 MPa, 3 min
ZrCoSb	No	30 h		1323 K, 50 MPa, 3 min
TiCoSb	Yes	2 h		1373 K, 50 MPa, 5 min
NbFeSb	No	20 h		1223 K, 50 MPa, 3 min
TaFeSb	No	30 h		1173 K, 50 MPa, 3 min
NbCoSn	No	20 h		1173 K, 50 MPa, 3 min
ZrNiSn	Yes	2 h		1273 K, 50 MPa, 3 min
TiNiSn	Yes	2 h		1273 K, 70 MPa, 2 min
Zr _{0.7} Ti _{0.3} CoSb	No	30 h		1323 K, 50 MPa, 3 min
ZrCoSb _{0.8} Sn _{0.2}	No	30 h		1323 K, 50 MPa, 3 min

electron microscope (TEM) investigations were prepared by mechanical polishing, dimpling, and then ion milling with liquid nitrogen stage. STEM imaging was carried out with JEOL ARM 200F equipped with double aberration correction. Selected samples for the Rietveld analyses were hand-milled in an agate mortar and a pestle. The powders were fixed between two polyacetate films and glued with a mixture of amyl acetate and collodion. The X-ray diffraction patterns were obtained by a STOE Stadi P diffractometer with a Mo source and a Ge(111) monochromator which yielded a single wavelength of 0.7093 Å. The Rietveld analyses^[37] were performed using Fullprof implemented in the WinPlotR software environment.^[38] The structure model of Romaka et al. for ZrCoSb with the space group $F\bar{4}3m$ (No. 216) was adapted to HfCoSb.^[39] The structure model of the minor phase CoSb with the space group $P6_3/mmc$ (No. 194) was taken from the same reference. Beside typical parameters at $nP_r = 7$ for the structure model refinement, an overall temperature factor (B_{ov}), asymmetry parameters Asy1 and Asy2 and U for microstructure contributions were refined. To evaluate the concentration of the Co interstitial/vacancy pairs, the occupancies of the Co/4c and Co/4d sites were refined simultaneously.

The thermal conductivity, κ , was calculated as the multiplication of the thermal diffusivity (D), mass density (d), and the specific heat (c_p). The thermal diffusivity and the mass density were measured by a Laserflash analyzer (LFA1000, Linseis) and an Archimedes kit, respectively. The specific heat was calculated using the Dulong–Petit law. The electrical conductivity and the Seebeck coefficient of ZrCoSb_{0.8}Sn_{0.2} were measured by a commercial device (LSR-3, Linseis). The measurement uncertainties were 4%, 5%, and 12% for electrical conductivity, the Seebeck coefficient, and the thermal conductivity, respectively. To increase the readability of the graphs, the error bars on the curves were not added.

The formation energy of different defects and electronic calculations in this work were based on DFT implemented in the Vienna Ab-initio Simulation Package.^[40,41] A supercell consisting of 27 ($3 \times 3 \times 3$) chemical units was adopted for structural relaxation and phonon calculations. The elements were represented by projector-augmented wave potentials^[42,43] with 350 eV energy cutoff and the 12 valence electrons for Zr ($4s^2 4p^6 5s^2 4d^2$); 9 for Co ($3d^7 4s^2$); 5 for Sb ($5s^2 5p^3$); and 10 for Hf ($5p^6 5d^2 6s^2$) were treated explicitly. Initial relaxation and energetics were calculated via the generalized gradient approximation of Perdew–Burke–Ernzerhof functionals.^[44] The first Brillouin zone was sampled by the tetrahedron method on a gamma-centered $8 \times 8 \times 8$ k -mesh. All structures were relaxed until the force on each atom was less than $0.01 \text{ meV \AA}^{-1}$.

Using density functional theory, the dispersion relations and modal scattering rate were calculated. These required second-order and third-order interatomic force constants (IFCs), denoted by $\Phi_{\lambda,\lambda'}$ and $\Phi_{\lambda,\lambda',\lambda''}$. For this purpose, the finite displacement technique was applied, implemented in Phonopy^[45] and Phono3py,^[46] respectively. For the second-order IFC calculations, to construct the dynamical matrices, each atom was displaced by 0.01 \AA in $3 \times 3 \times 3$ supercells (81 atoms). A Γ -centered $15 \times 15 \times 15$ k -mesh was used for Brillouin zone sampling. For the third-order IFC calculations, a $3 \times 3 \times 3$ supercell, atomic displacements of 0.03 \AA , and a $45 \times 45 \times 45$ k -grid were used. For both second-order and third-order IFCs, density functional theory was used as described above for total energy calculations.

Given the third-order IFCs, the three-phonon scattering rate $1/\tau_\lambda$ can be formulated based on the Fermi's golden rule

$$\frac{1}{\tau_\lambda} = \frac{36\pi}{\hbar^2} \sum_{\lambda'\lambda''} |\phi_{\lambda\lambda'\lambda''}|^2 \times (n_{\lambda'}^0 + n_{\lambda''}^0 + 1) \delta(\omega_\lambda - \omega_{\lambda'} - \omega_{\lambda''}) + (n_{\lambda'}^0 - n_{\lambda''}^0) [\delta(\omega_\lambda + \omega_{\lambda'} - \omega_{\lambda''}) - \delta(\omega_\lambda - \omega_{\lambda'} + \omega_{\lambda''})] \quad (1)$$

where λ indicates phonon mode (q, j), n^0 is the Bose–Einstein distribution, and the delta function $\delta(\cdot)$ enforces energy conservation during scattering. The formalism of Fermi's golden rule was consistent with the single-mode relaxation time approximation (RTA) of the Boltzmann equation. Both of these assumed the single-particle transport picture. In the RTA, the lattice thermal conductivity is defined as

$$\kappa = \frac{1}{V} \sum_{\lambda} C_{\lambda} \mathbf{v}_{\lambda} \otimes \mathbf{v}_{\lambda} \tau_{\lambda} \quad (2)$$

where V is the volume, $C_{\lambda} = k_B x \exp(x) / (\exp(x) - 1)$ is modal heat capacity, $x = \hbar\omega_{\lambda}/k_B T$, $\mathbf{v}_{\lambda} = \partial\omega_{\lambda}/\partial \mathbf{q}_{\lambda}$ and τ_{λ} are the group velocity and relaxation time for mode λ , and \mathbf{q}_{λ} is its wavevector. In this definition

$$\mathbf{v} \otimes \mathbf{v} = \begin{bmatrix} v_x v_x & v_x v_y & v_x v_z \\ v_y v_x & v_y v_y & v_y v_z \\ v_z v_x & v_z v_y & v_z v_z \end{bmatrix} \quad (3)$$

is the tensor product of group velocity $\mathbf{v} = (v_x, v_y, v_z)$. In this work, the reported thermal conductivity was a scalar, $\kappa = \text{tr}(\boldsymbol{\kappa})/3 = (\kappa_{xx} + \kappa_{yy} + \kappa_{zz})/3$, where κ_{xx} , κ_{yy} and κ_{zz} are the diagonal terms of $\boldsymbol{\kappa}$.

3. Results and Discussion

High-purity half-Heusler phases are obtained with HP sintering, as examined by X-ray diffraction (XRD) and shown in Figure S1 (Supporting Information). The final densities of the half-Heusler compounds are listed in Table S1 (Supporting Information). The HP compounds possess densities comparable to the HT-prepared ones and exceed 95% of the theoretical density from the X-ray diffraction patterns. Therefore, the change in the density affects the final κ value negligibly. Figure 2a,b shows the κ values of the eight pristine half-Heusler compounds that are prepared by either HP or HT sintering. Note that $\kappa \approx \kappa_{\perp}$ applies for these compounds that are not doped alicovalently unless bipolar conduction is excited. Reduction in κ_{\perp} is realized for all the Sb-based compounds with a maximum rate of $\approx 83\%$ for HfCoSb at 300 K from 14.5 to $2.5 \text{ W m}^{-1} \text{ K}^{-1}$, as shown in Figure 2c. Except for the severe deformation as realized by Masuda et al. and Rogl et al. through high-pressure torsion,^[47,48] such reduction rate was scarcely observed for bulk compounds by applying high-pressure sintering for other materials even with much higher sintering pressure. For example, Cai et al. reported a κ_{\perp} reduction of $\approx 20\%$ for Na-doped PbTe with a much higher sintering pressure of 6 GPa at 1073 K.^[49] In another example, a reduction of

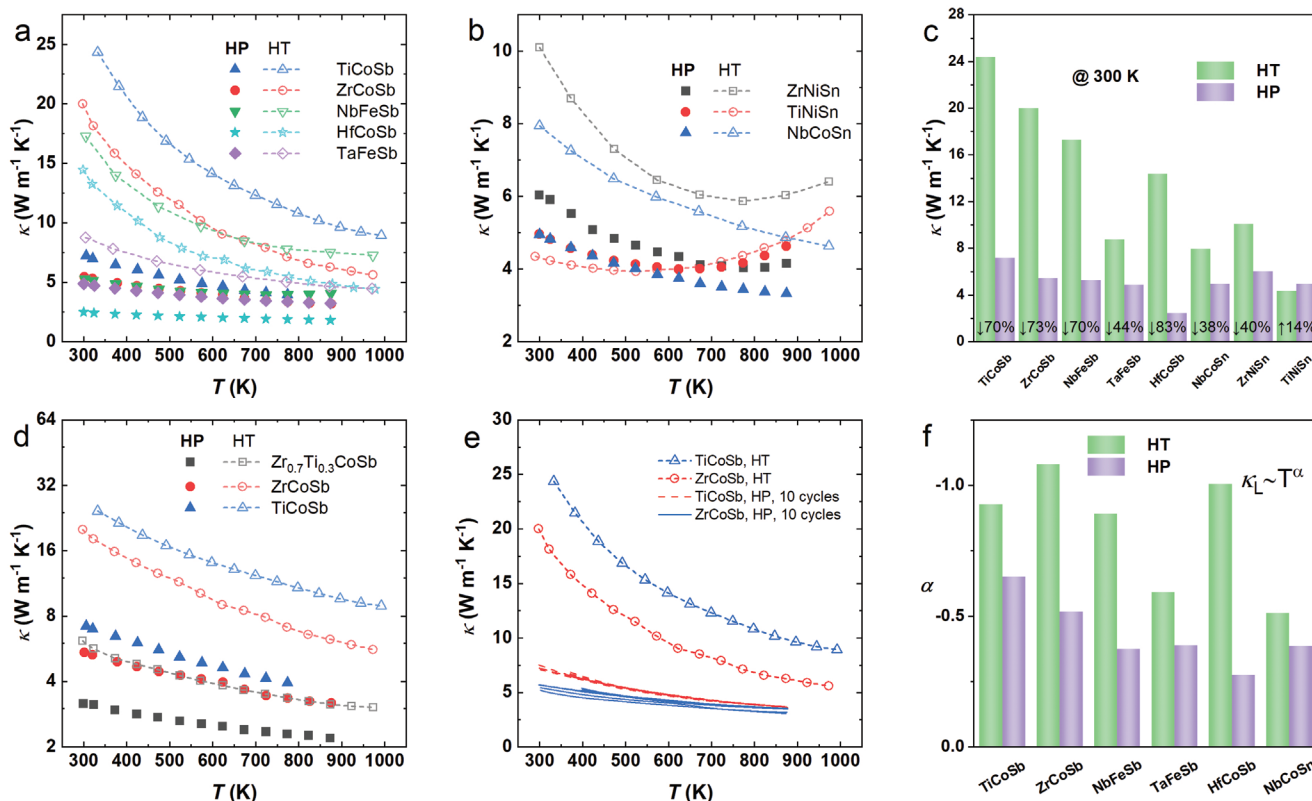


Figure 2. Thermal-conductivity comparisons of half-Heusler (HH) compounds that are sintered under high pressure (HP) or high temperature (HT). Temperature-dependent thermal conductivity of a) Sb-based and b) Sn-based compounds. c) The reduction of thermal conductivity of eight pristine HH compounds at 300 K. Temperature-dependent thermal conductivity of ZrCoSb and TiCoSb with d) alloyed $\text{Zr}_{0.7}\text{Ti}_{0.3}\text{CoSb}$ and e) cycling test for 10 times. f) The index α as in $\kappa_L \propto T^\alpha$ for the HP- and HT-sintered compounds.

$\approx 30\%$ was realized for the κ_L values in thermoelectric BiCuSeO upon applying a 3 GPa pressure under 973 K.^[50] We thus emphasize the importance of a combination of high sintering pressure and reduced sintering temperature to realize the drastic reduction of κ_L . Furthermore, applying HP also reduces the κ values of some Sn-based compounds including ZrNiSn and NbCoSn with a relatively smaller reduction rate of $\approx 40\%$ at 300 K. However, the κ of TiNiSn are almost identical between the HP and HT compounds, suggesting that the microstructural features of TiNiSn are not sensitive to the sintering conditions applied herein. The similar κ curves of TiNiSn help to understand the heat transport properties. Following a previous report, the phonon scattering in TiNiSn is dominated by interstitial Ni point defects.^[12] As will be discussed later, we verify that this mechanism is indeed contributing to the reduced κ_L for the HP compounds, such as HfCoSb.

The κ_L reductions, especially for the Sb-based half-Heusler compounds are remarkable due to the large reduction rate and, as the main reason, the simple modification of the sintering conditions to higher pressure at a lower temperature. Besides, we compare the κ_L values among ZrCoSb, TiCoSb, and $\text{Zr}_{0.7}\text{Ti}_{0.3}\text{CoSb}$ that are prepared by either the HP or the HT method. A similar κ_L reduction is achieved for $\text{Zr}_{0.7}\text{Ti}_{0.3}\text{CoSb}$. For example, as shown in Figure 2d, the κ_L value of the HT-sintered $\text{Zr}_{0.7}\text{Ti}_{0.3}\text{CoSb}$ is $\approx 6.2 \text{ W m}^{-1} \text{K}^{-1}$ at 300 K, while it drops by $\approx 50\%$ to $\approx 3.2 \text{ W m}^{-1} \text{K}^{-1}$ for the same nominal

composition prepared with the HP method. Therefore, isoelectric substitution and high-pressure sintering are combined to concertedly reduce the κ_L property of our materials, which indicates the potential to become a routine for further κ_L reduction. Moreover, as shown in Figure 2e, the respective κ_L curves of TiCoSb and ZrCoSb almost overlap among the tenfold-repeated measurements to 873 K, thus confirming a well-preserved κ_L reduction as long as the measurement temperature does not exceed the sintering temperature (923 K).

The phonon scattering mechanism is estimated by the index α in $\kappa_L \propto T^\alpha$. Theoretically, the respective values of α are -1 and -0.5 if phonons are mainly scattered by the intrinsic phonon-phonon interaction or point defects.^[18] Besides, the boundary-dominant phonon scattering is usually observed at cryogenic temperatures with the theoretical value of α being either 3 or 2 depending on the assumption whether the scattering rate is phonon-frequency sensitive.^[51] In some special cases such as nanowires, positive values of α are obtained at above 300 K,^[52] thus manifesting the role of boundary scattering in increasing α (i.e., decreasing the $|\alpha|$). The α values of HfCoSb, ZrCoSb, TiCoSb, NbFeSb, TaFeSb, and NbCoSn are plotted in Figure 2f, whereas ZrNiSn and TiNiSn are not included because of their obvious bipolar thermic conduction upon heating. A consistent improvement of α is obtained for the selected compounds. Especially, an increased α of -0.28 is observed on HfCoSb that deviates from the values of phonon-phonon interaction (-1) or

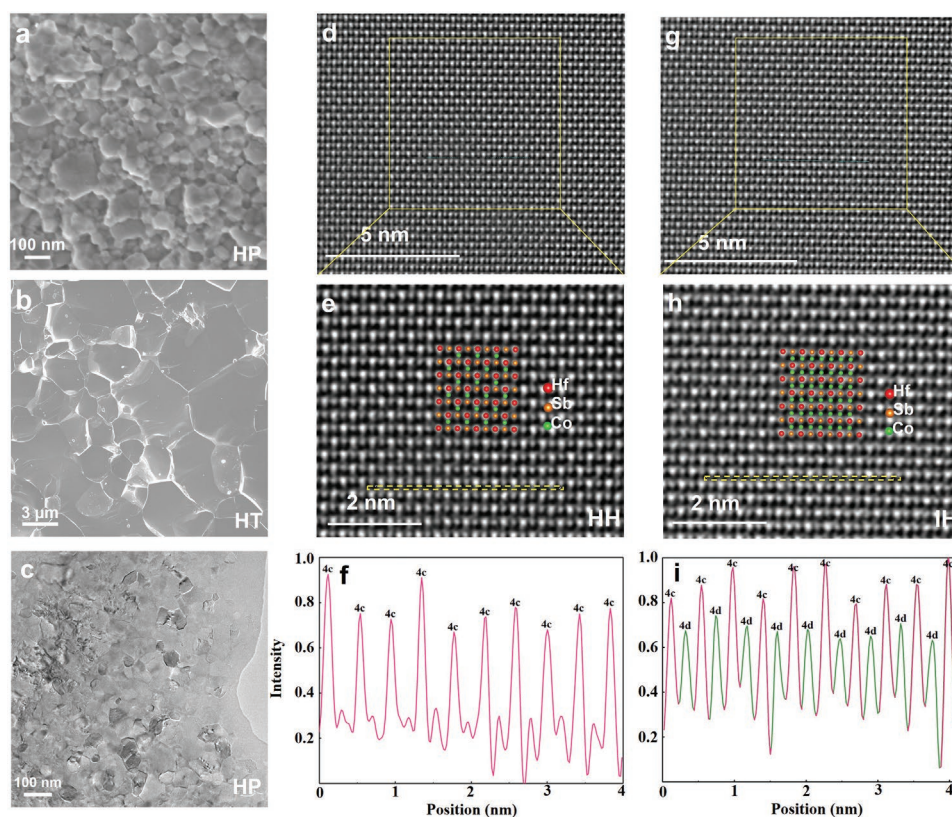


Figure 3. Microscopy investigations of HfCoSb. SEM images of the broken surfaces of HfCoSb that are sintered through a) high pressure or b) high temperature. c) Low-magnification TEM images of the HP-sintered HfCoSb. HAADF-STEM images of HP-sintered HfCoSb at different regions, showing the coexistence of d,e) HH and g,h) intermediate-Heusler (IH) phases. f,i) The intensity profiles for the 4c/4d sites, as shown in the yellow boxes in (e) and (h), are shown.

point-defect scattering (~ 0.5). Such an increase in α suggests another major mechanism in scattering phonons, possibly from the grain boundaries. To further understand the defect characteristics, we performed microscopic studies for the structural origins of the enhanced phonon scattering.

The reduced sintering temperature yields a drastic grain refinement. Taking HfCoSb as an example, **Figure 3a** shows the scanning electron microscope (SEM) images of the broken surfaces of the HfCoSb compounds that are subject to HP sintering. A statistical analysis following the SEM characterization suggested an area-weighted grain size of ≈ 94.4 (± 28.8) nm with HP, thus confirming a grain refinement of more than one order of magnitude compared to the HT specimen with $\approx 1\text{--}10$ μm , as shown in **Figure 3b**. The sub-100 nm average grain size is further confirmed by low-resolution transmission electron microscope (TEM) investigations, as shown in **Figure 3c**. Therefore, the grain-boundary scattering is believably one significant contributor to the enhanced phonon scattering.

For compounds that are synthesized through high pressure, strong lattice disorder is expected. To characterize the structural features of the compounds, sintered in this work through high pressure on the atomic level, we perform a spherical-aberration-corrected (C_s) scanning transmission electron microscopy (STEM) investigation using JEM-ARM 200F on HfCoSb because it displays the largest κ_L reduction. Note that the thermoelectric half-Heusler compounds crystallize in space group $F\bar{4}3m$

(No. 216) with three interpenetrating face-centered cubic (fcc) sublattices. They possess a nominal formula XYZ with X elements being early transition metals (Zr, Hf, etc.), Y being late transition metals (Co, Ni, etc.), and Z being main group metals or metalloids (Sn, Sb, etc.). The X, Y, Z elements ideally occupy the Wyckoff positions 4b ($1/2, 1/2, 1/2$), 4c ($1/4, 1/4, 1/4$), and 4a (0,0,0), respectively, and leaving the remaining 4d ($3/4, 3/4, 3/4$) sites as tetrahedral vacancies. For the HfCoSb sample, the different Wyckoff positions do not overlap in the [110] structural projection. **Figure 3d,g** shows [110] high-angle annular dark-field (HAADF)-STEM images in which the Hf, Co, and Sb atomic columns are revealed individually. By magnifying the HAADF-STEM images, we find distinct atomic occupation features wherein **Figure 3e,h** the 4d sites are empty and occupied, respectively. We further evaluate the integrating intensity of two 4c/4d planes in both regions, as indicated by the two yellow boxes in **Figure 3e,h**. The respective intensities are shown in **Figure 3f,i**. Note that in **Figure 3f** the small extrema at the 4d sites originate from overlapped profiles between the neighboring 4c sites instead of from occupation. The intensities among the 4c sites are not uniform, suggesting the existence of Co vacancies. By contrast, **Figure 3i** shows a partial occupation of both 4c and 4d sites, featuring an intermediate-Heusler phase. Following our previous work, these 4d lattice sites are occupied by Co atoms due to their lowest formation energy.^[18] We thus verify a coexistence of half-Heusler (HH) and

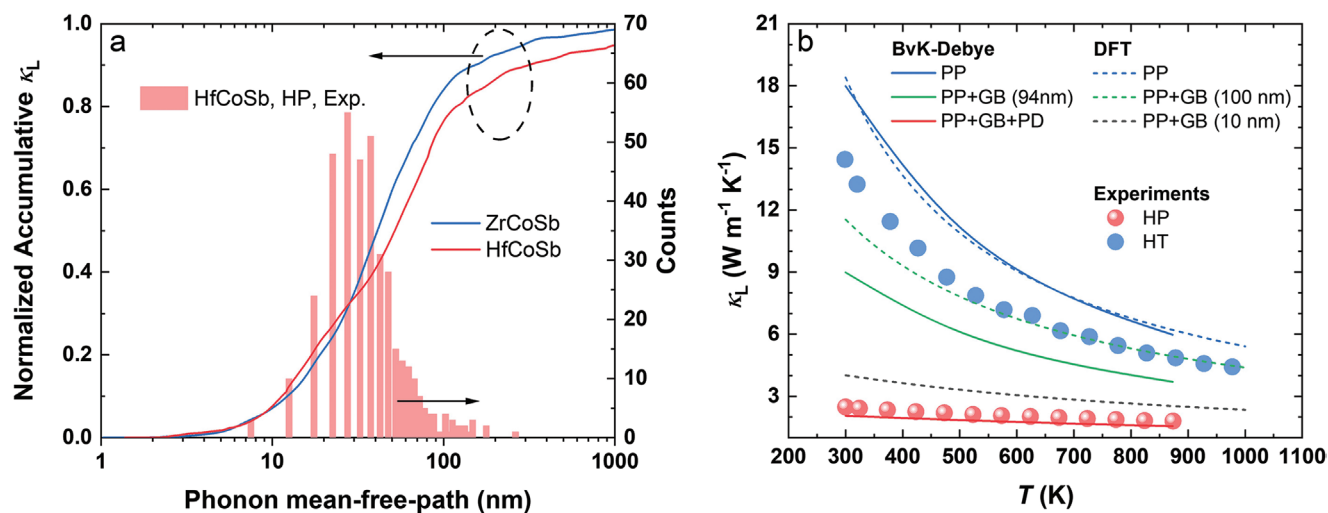


Figure 4. a) Phonon mean-free-path-dependent normalized accumulative lattice thermal conductivity of HfCoSb and ZrCoSb overlapping the grain size distribution of HfCoSb. b) Temperature-dependent lattice thermal conductivity of HfCoSb through DFT calculations or BvK–Debye modeling. The experimental values are plotted for comparison. The labels PP, GB, and PD represent phonon–phonon interaction, grain-boundary scattering, and point-defect scattering, respectively.

intermediate-Heusler (IH) phases, but not a full-Heusler (FH) phase. This behavior is different from the Ni-based compounds such as ZrNiSn where HH, IH, FH phases were observed simultaneously.^[53] Indeed, unlike MNi₂Sn (M = Hf, Zr, or Ti), there is no record of full-Heusler MCo₂Sb compounds, e.g., in the Inorganic Crystal Structure Database or the Crystallography Open Database.

Subsequently, to evaluate the concentration of Co interstitial/vacancy pairs (Co/4d) in the HP-sintered HfCoSb, we compare the Rietveld analyses results based on powder XRD with/without Co/4d defects under the constraint that the total occupancy for both Co sites is 100%. As shown in Figure S3 (Supporting Information), high-quality fits are realized even without including any defects, showing a good crystallinity of the HP-sintered compound. Allowing a flexible migration between 4c and 4d lattice sites further improves the fit quality with an $\approx 2.3\%$ concentration of Co/4d defects, thus evidencing the atomic disorder. The refined concentration of defects is considerable in scattering phonons due to the involvement of vacancies and interstitials, as similarly discussed in ZrCoSb-based compounds.^[18] Overall, our structural investigations uncover the abundant concentration of 0D point defects and 2D grain boundaries. These defects will be shown to be accountable for the remarkably reduced κ_L through phonon-transport analysis.

Density-functional-theory (DFT) calculations are applied to access the scattering from the grain boundaries. The computation details are discussed in the “Experimental Section.” Figure 4a shows the mean-free-path-dependent accumulated, normalized κ_L of ZrCoSb and HfCoSb at 300 K. Obviously, most of the heat-conduction-related phonons possess a mean free path in between a few tens of nanometers for both compounds. Note that the result of ZrCoSb is similar to the previous calculations from Zhou et al. and Shiomi et al., thus verifying the reliability of our calculations.^[54,55] Besides, we overlap the grain-size distribution of HfCoSb with HP sintering in Figure 4a. The grain sizes with a higher count coincide with the mean free paths of phonons that are most contributing to the heat transport, thus

suggesting an effective phonon scattering from grain boundaries. Furthermore, Figure 4b shows the calculated temperature-dependent κ_L of HfCoSb based on either DFT or the BvK–Debye model. The modeling details were introduced in our previous work,^[18] and the modeling parameters (such as the longitudinal and transverse speed of sound) take literature values.^[56] For boundary-free compounds (i.e., only the phonon–phonon interactions present), the κ_L from DFT and BvK–Debye show excellent agreement. Applying a grain size of 100 nm and assuming a mode-dependent scattering rate from boundaries, the DFT calculation generates a κ_L reduction of $\approx 40\%$. This finding is similar to the κ_L reduction of 50% calculated with the BvK–Debye model for a grain size of ≈ 94 nm. These results are consistent with our previous conclusions that a grain refinement to 100 nm and below is needed for effective phonon scattering.^[18]

Nevertheless, Figure 4b shows that, even by imposing a grain size of 10 nm, the DFT-calculated κ_L do not match the experimental κ_L of the HP HfCoSb. Therefore, other scattering mechanisms such as Co/4d point defects should be considered. The synergistic effects in phonon scattering from the various mechanisms are evaluated by the BvK–Debye model. Note that the Co/4d defect concentration is determined from a Rietveld analysis ($\approx 2.3\%$), so no random fitting parameter is employed in our modeling. As shown in Figure 4b, the modeled κ_L matches the experimental values well, thus confirming the synergistic phonon scattering from the 2D grain boundaries and the 0D point defects.

Because of the huge κ_L reduction, especially for the Sb-based compounds, the high-pressure sintering becomes very promising in improving the thermoelectric performance of half-Heusler compounds if the electronic transport is less perturbed. On the other hand, since the drastic reductions of κ_L are partially realized by a higher atomic disorder, it remains challenging to preserve the electrical conductivity (σ) due to the enhanced scattering from ionized impurities. It is desired that, at least, the reduction of the σ should be less than that in κ_L . To our opinion, four strategies can potentially succeed. First, heavily doped compounds are preferred over the lightly

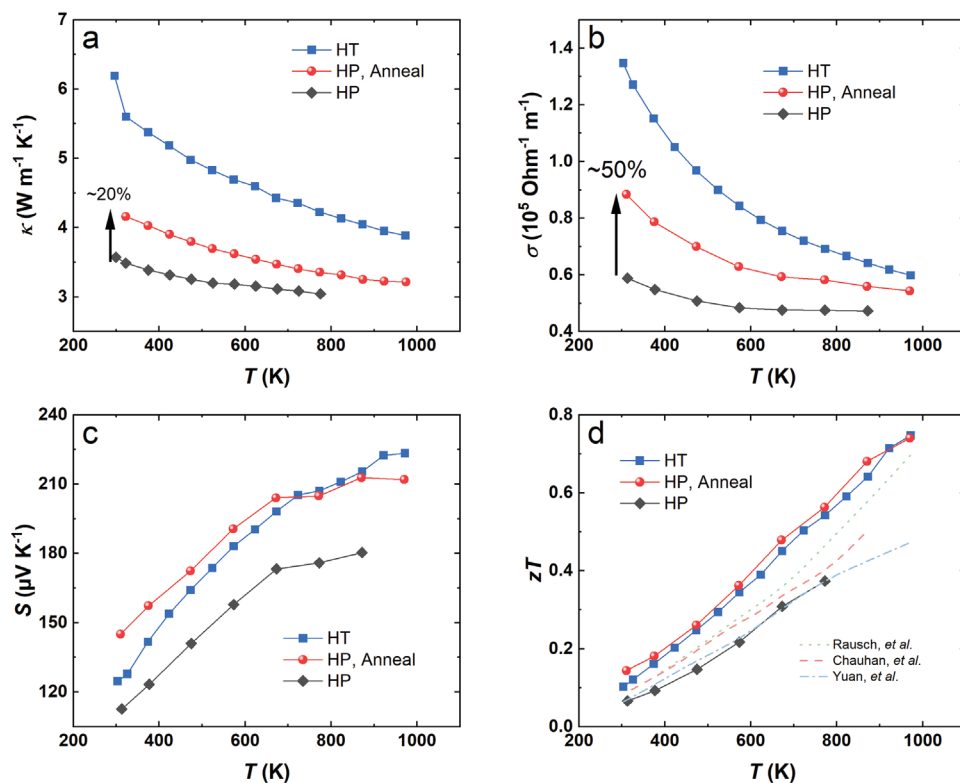


Figure 5. Temperature-dependent a) thermal conductivity, b) electrical conductivity, c) Seebeck coefficient, and d) zT of $\text{ZrCoSb}_{0.8}\text{Sn}_{0.2}$ that are sintered by either HT or HP with/without a postannealing. The zT of $\text{ZrCoSb}_{0.8}\text{Sn}_{0.2}$ from several previous reports are also included in (d).

doped ones, since a higher Hall carrier concentration can potentially shield the Coulomb potential from the ionized scattering centers. In this sense, the half-Heusler compounds are preferred candidates for HP sintering since their optimized carrier concentrations are usually high ($>10^{21} \text{ cm}^{-3}$).

Second, the thermoelectric performance is usually optimized through a trade-off between the transport of electrons and phonons. Therefore, a postannealing is potentially beneficial to optimize the σ/κ_L ratio by partially recovering these localized, ionized centers. This procedure was successfully demonstrated in our preliminary studies of a doped composition, $\text{ZrCoSb}_{0.8}\text{Sn}_{0.2}$. As shown in Figure 5a,b, by annealing this compound at 1073 K for 30 min. in vacuum, both the electrical and the thermal transport are recovered. Importantly, the recovery rate of the electrical conductivity is $\approx 50\%$, much larger than the $\approx 20\%$ of the thermal conductivity, so the σ/κ_L ratio is improved. The σ/κ_L ratio can be further improved by optimizing the annealing condition.

Third, Figure 5a displays that although the κ_L increases upon annealing, it remains $\approx 33\%$ lower than the HT-sintered sample at 300 K. Besides, as already shown in Figure 2d, the κ_L can be reduced through alloying such as among Hf/Zr/Ti. This approach is expected to less interfere with the transport of charge carriers since these elements are isovalent.

Finally, as shown in Figure 5c, the Seebeck coefficient of the annealed HP compound enhances or reduces unexpectedly below or above 700 K when compared to the HT sample. There are several possible explanations for the Seebeck anomaly such as an insufficient dopant activation, a modified scattering

mechanism, or an energy filter effect from quantum confinement due to the refined grain size, etc. The exotic transport properties demand subsequent analysis for an explanation. Nevertheless, the enhanced Seebeck coefficient further justifies the beneficial effects of high-pressure sintering. As shown in Figure 5d, the resulting zT values of the high pressure-sintered $\text{ZrCoSb}_{0.8}\text{Sn}_{0.2}$ following annealing slightly exceed that of the high temperature-sintered compound and are higher than the results from previous reports.^[28,57,58] More importantly, upon HP sintering and annealing, the individual parameters (the two conductivities and the Seebeck coefficient) are distinct from the high-temperature-sintered counterparts. Therefore, our synthesis approach opens up the possibility to decouple the transport of electrons and phonons, which merits an extended investigation of high-pressure sintering for better thermoelectric performance.

4. Conclusion

In summary, we report the effects of microstructural modification in tailoring the phonon transport properties of half-Heusler compounds that are synthesized through sintering under high pressure (1 GPa) but with reduced temperature (923 K). We show the drastic reduction of the lattice thermal conductivity for most compositions in this work with a maximum reduction reaching $\approx 83\%$ for HfCoSb at 300 K. The obtained properties are preserved under repeated measurements and are combined with other phonon-scattering approaches such as alloying. Through microscopy analysis on HfCoSb, we describe detailed structural

features including a grain refinement to below 100 nm and the simultaneous occupation of 4c and 4d lattice sites, which is further quantified by Rietveld analyses. These quantified defects are well correlated to the lattice thermal conductivity following phonon-transport calculations, thus justifying a synergistic phonon scattering effect. Moreover, our results on electronic transport show beneficial changes in the Seebeck coefficient, albeit further studies are needed for understanding. We also outlook the potential strategies such as annealing that can increase the electrical-to-thermal-conductivity ratio for a zT optimization. Overall, owing to the capability of broadening the possible microscopic states of half-Heusler compounds, high-pressure sintering offers new chances to tailor the individual transport behaviors, especially the phonon scattering to an unusual degree. Our work thus indicates the great potential of high-pressure-sintering-induced microstructural engineering for improving the thermoelectric performance for half-Heusler compounds and possibly other materials.

Supporting Information

Supporting Information is available from the Wiley Online Library or from the author.

Acknowledgements

R.H., T.Z., and P.Y. contributed equally to this work. P.Y. acknowledges the financial support from the strategic project at IFW Dresden on "Wireless sensor devices for high temperature applications." Y.W. acknowledges the financial support from the National Natural Science Foundation of China (Grant No. 12074409).

Open access funding enabled and organized by Projekt DEAL.

Conflict of Interest

The authors declare no conflict of interest.

Data Availability Statement

Research data are not shared.

Keywords

half-Heusler compounds, high-pressure sintering, lattice thermal conductivity, thermoelectric devices

Received: April 13, 2021

Revised: April 19, 2021

Published online: July 8, 2021

- [1] W. Wang, V. Cionca, N. Wang, M. Hayes, B. O'Flynn, C. O'Mathuna, *Int. J. Distrib. Sens. Networks* **2013**, *9*, 232438.
- [2] G. Li, J. Garcia Fernandez, D. A. Lara Ramos, V. Barati, N. Pérez, I. Soldatov, H. Reith, G. Schierning, K. Nielsch, *Nat. Electron.* **2018**, *1*, 555.

- [3] B. Poudel, Q. Hao, Y. Ma, Y. Lan, A. Minnich, B. Yu, X. Yan, D. Wang, A. Muto, D. Vashaee, X. Chen, J. Liu, M. S. Dresselhaus, G. Chen, Z. Ren, *Science* **2008**, *320*, 634.
- [4] S. Pan, L. Liu, Z. Li, X. Yan, C. Wang, K. Guo, J. Yang, Y. Jiang, J. Luo, W. Zhang, *Mater. Today Phys.* **2021**, *17*, 100333.
- [5] Y. Pan, U. Aydemir, J. A. Grovogui, I. T. Witting, R. Hanus, Y. Xu, J. Wu, C.-F. Wu, F.-H. Sun, H.-L. Zhuang, J.-F. Dong, J.-F. Li, V. P. Dravid, G. J. Snyder, *Adv. Mater.* **2018**, *30*, 1802016.
- [6] S. Li, Y. Liu, F. Liu, D. He, J. He, J. Luo, Y. Xiao, F. Pan, *Nano Energy* **2018**, *49*, 257.
- [7] Q. Zhang, E. K. Chere, Y. Wang, H. S. Kim, R. He, F. Cao, K. Dahal, D. Broido, G. Chen, Z. Ren, *Nano Energy* **2016**, *22*, 572.
- [8] Y. Luo, J. Yang, Q. Jiang, W. Li, Y. Xiao, L. Fu, D. Zhang, Z. Zhou, Y. Cheng, *Nano Energy* **2015**, *18*, 37.
- [9] Z. Chen, Z. Jian, W. Li, Y. Chang, B. Ge, R. Hanus, J. Yang, Y. Chen, M. Huang, G. J. Snyder, Y. Pei, *Adv. Mater.* **2017**, *29*, 1606768.
- [10] F. Guo, B. Cui, Y. Liu, X. Meng, J. Cao, Y. Zhang, R. He, W. Liu, H. Wu, S. J. Pennycook, W. Cai, J. Sui, *Small* **2018**, *14*, 1802615.
- [11] R. He, D. Kraemer, J. Mao, L. Zeng, Q. Jie, Y. Lan, C. Li, J. Shuai, H. S. Kim, Y. Liu, D. Broido, C.-W. Chu, G. Chen, Z. Ren, *Proc. Natl. Acad. Sci. USA* **2016**, *113*, 13576.
- [12] W. Ren, H. Zhu, J. Mao, L. You, S. Song, T. Tong, J. Bao, J. Luo, Z. Wang, Z. Ren, *Adv. Electron. Mater.* **2019**, *5*, 1900166.
- [13] W. Ren, H. Zhu, Q. Zhu, U. Saparamadu, R. He, Z. Liu, J. Mao, C. Wang, K. Nielsch, Z. Wang, Z. Ren, *Adv. Sci.* **2018**, *5*, 1800278.
- [14] M. Gürth, G. Rogl, V. V. Romaka, A. Grytsiv, E. Bauer, P. Rogl, *Acta Mater.* **2016**, *104*, 210.
- [15] G. Rogl, A. Grytsiv, M. Gürth, A. Tavassoli, C. Ebner, A. Wünschek, S. Puchegger, V. Soprunyuk, W. Schranz, E. Bauer, H. Müller, M. Zehetbauer, P. Rogl, *Acta Mater.* **2016**, *107*, 178.
- [16] R. He, S. Gahlawat, C. Guo, S. Chen, T. Dahal, H. Zhang, W. Liu, Q. Zhang, E. Chere, K. White, Z. Ren, *Phys. Status Solidi A* **2015**, *212*, 2191.
- [17] M. W. Gaultois, T. D. Sparks, *Appl. Phys. Lett.* **2014**, *104*, 113906.
- [18] R. He, T. Zhu, Y. Wang, U. Wolff, J.-C. Jaud, A. Sotnikov, P. Potapov, D. Wolf, P. Ying, M. Wood, Z. Liu, L. Feng, N. P. Rodriguez, G. J. Snyder, J. C. Grossman, K. Nielsch, G. Schierning, *Energy Environ. Sci.* **2020**, *13*, 5165.
- [19] Y. Pan, Y. Qiu, I. Witting, L. Zhang, C. Fu, J.-W. Li, Y. Huang, F.-H. Sun, J. He, G. J. Snyder, C. Felser, J.-F. Li, *Energy Environ. Sci.* **2019**, *12*, 624.
- [20] H. Zhao, J. Sui, Z. Tang, Y. Lan, Q. Jie, D. Kraemer, K. McEnaney, A. Guloy, G. Chen, Z. Ren, *Nano Energy* **2014**, *7*, 97.
- [21] H. Zhu, J. Mao, Y. Li, J. Sun, Y. Wang, Q. Zhu, G. Li, Q. Song, J. Zhou, Y. Fu, R. He, T. Tong, Z. Liu, W. Ren, L. You, Z. Wang, J. Luo, A. Sotnikov, J. Bao, K. Nielsch, G. Chen, D. J. Singh, Z. Ren, *Nat. Commun.* **2019**, *10*, 270.
- [22] J. Yu, C. Fu, Y. Liu, K. Xia, U. Aydemir, T. C. Chasapis, G. J. Snyder, X. Zhao, T. Zhu, *Adv. Energy Mater.* **2018**, *8*, 1701313.
- [23] C. Fu, T. Zhu, Y. Liu, H. Xie, X. Zhao, *Energy Environ. Sci.* **2015**, *8*, 216.
- [24] C. Fu, S. Bai, Y. Liu, Y. Tang, L. Chen, X. Zhao, T. Zhu, *Nat. Commun.* **2015**, *6*, 8144.
- [25] H. Zhu, R. He, J. Mao, Q. Zhu, C. Li, J. Sun, W. Ren, Y. Wang, Z. Liu, Z. Tang, A. Sotnikov, Z. Wang, D. Broido, D. J. Singh, G. Chen, K. Nielsch, Z. Ren, *Nat. Commun.* **2018**, *9*, 2497.
- [26] Y. Xing, R. Liu, J. Liao, Q. Zhang, X. Xia, C. Wang, H. Huang, J. Chu, M. Gu, T. Zhu, C. Zhu, F. Xu, D. Yao, Y. Zeng, S. Bai, C. Uher, L. Chen, *Energy Environ. Sci.* **2019**, *12*, 3390.
- [27] W. Ren, Q. Song, H. Zhu, J. Mao, L. You, G. A. Gamage, J. Zhou, T. Zhou, J. Jiang, C. Wang, J. Luo, J. Wu, Z. Wang, G. Chen, Z. Ren, *Mater. Today Phys.* **2020**, *15*, 100250.
- [28] E. Rausch, B. Balke, S. Ouardi, C. Felser, *Phys. Chem. Chem. Phys.* **2014**, *16*, 25258.
- [29] Y. Liu, C. Fu, K. Xia, J. Yu, X. Zhao, H. Pan, C. Felser, T. Zhu, *Adv. Mater.* **2018**, *30*, 1800881.

- [30] C. Hu, K. Xia, X. Chen, X. Zhao, T. Zhu, *Mater. Today Phys.* **2018**, *7*, 69.
- [31] R. He, H. Zhu, J. Sun, J. Mao, H. Reith, S. Chen, G. Schierning, K. Nielsch, Z. Ren, *Mater. Today Phys.* **2017**, *1*, 24.
- [32] G. Rogl, P. Sauerschnig, Z. Rykavets, V. V. Romaka, P. Heinrich, B. Hinterleitner, A. Grytsiv, E. Bauer, P. Rogl, *Acta Mater.* **2017**, *131*, 336.
- [33] J. Mao, J. Zhou, H. Zhu, Z. Liu, H. Zhang, R. He, G. Chen, Z. Ren, *Chem. Mater.* **2017**, *29*, 867.
- [34] S. Li, H. Zhu, J. Mao, Z. Feng, X. Li, C. Chen, F. Cao, X. Liu, D. J. Singh, Z. Ren, Q. Zhang, *ACS Appl. Mater. Interfaces* **2019**, *11*, 41321.
- [35] R. He, L. Huang, Y. Wang, G. Samsonidze, B. Kozinsky, Q. Zhang, Z. Ren, *APL Mater.* **2016**, *4*, 104804.
- [36] F. Serrano-Sánchez, T. Luo, J. Yu, W. Xie, C. Le, G. Auffermann, A. Weidenkaff, T. Zhu, X. Zhao, J. A. Alonso, B. Gault, C. Felser, C. Fu, *J. Mater. Chem. A* **2020**, *8*, 14822.
- [37] H. M. Rietveld, *J. Appl. Crystallogr.* **1969**, *2*, 65.
- [38] T. Roisnel, J. Rodríguez-Carvajal, *Mater. Sci. Forum* **2001**, *378–381*, 118.
- [39] V. V. Romaka, L. Romaka, P. Rogl, Y. Stadnyk, N. Melnychenko, R. Korzh, Z. Duriagina, A. Horyn, *J. Alloys Compd.* **2014**, *585*, 448.
- [40] G. Kresse, J. Furthmüller, *Phys. Rev. B* **1996**, *54*, 11169.
- [41] G. Kresse, J. Furthmüller, *Comput. Mater. Sci.* **1996**, *6*, 15.
- [42] P. E. Blöchl, *Phys. Rev. B* **1994**, *50*, 17953.
- [43] G. Kresse, D. Joubert, *Phys. Rev. B* **1999**, *59*, 1758.
- [44] J. P. Perdew, K. Burke, M. Ernzerhof, *Phys. Rev. Lett.* **1996**, *77*, 3865.
- [45] A. Togo, I. Tanaka, *Scr. Mater.* **2015**, *108*, 1.
- [46] A. Togo, L. Chaput, I. Tanaka, *Phys. Rev. B* **2015**, *91*, 094306.
- [47] S. Masuda, K. Tsuchiya, J. Qiang, H. Miyazaki, Y. Nishino, *J. Appl. Phys.* **2018**, *124*, 035106.
- [48] G. Rogl, S. Ghosh, L. Wang, J. Bursik, A. Grytsiv, M. Kerber, E. Bauer, R. C. Mallik, X.-Q. Chen, M. Zehetbauer, P. Rogl, *Acta Mater.* **2020**, *183*, 285.
- [49] B. Cai, J. Li, H. Sun, L. Zhang, B. Xu, W. Hu, D. Yu, J. He, Z. Zhao, Z. Liu, Y. Tian, *Sci. China Mater.* **2018**, *61*, 1218.
- [50] H. Zhu, Y. Li, H. Li, T. Su, C. Pu, Y. Zhao, Y. Ma, P. Zhu, X. Wang, *High Pressure Res.* **2016**, *37*, 36.
- [51] Z. Wang, J. E. Alaniz, W. Jang, J. E. Garay, C. Dames, *Nano Lett.* **2011**, *11*, 2206.
- [52] D. Li, Y. Wu, P. Kim, L. Shi, P. Yang, A. Majumdar, *Appl. Phys. Lett.* **2003**, *83*, 2934.
- [53] X. Li, P. Yang, Y. Wang, Z. Zhang, D. Qin, W. Xue, C. Chen, Y. Huang, X. Xie, X. Wang, M. Yang, C. Wang, F. Cao, J. Sui, X. Liu, Q. Zhang, *Research* **2020**, *2020*, 4630948.
- [54] J. Zhou, H. Zhu, T.-H. Liu, Q. Song, R. He, J. Mao, Z. Liu, W. Ren, B. Liao, D. J. Singh, Z. Ren, G. Chen, *Nat. Commun.* **2018**, *9*, 1721.
- [55] J. Shiomi, K. Esfarjani, G. Chen, *Phys. Rev. B* **2011**, *84*, 104302.
- [56] T. Sekimoto, K. Kurosaki, H. Muta, S. Yamasaka, *Int. Conf. Thermo-electr.* **2005**, *2005*, 347.
- [57] N. S. Chauhan, S. Bathula, B. Gahtori, Y. V. Kolen'ko, R. Shyam, N. K. Upadhyay, A. Dhar, *J. Appl. Phys.* **2019**, *126*, 125110.
- [58] B. Yuan, B. Wang, L. Huang, X. Lei, L. Zhao, C. Wang, Q. Zhang, *J. Electron. Mater.* **2016**, *46*, 3076.